Renewable Energy 199 (2022) 335–350

Contents lists available at ScienceDirect

Renewable Energy

journal homepage: www.elsevier.com/locate/renene

Performance analyses and heat transfer optimization of parabolic trough receiver with a novel single conical strip insert

Gen Ou [a], Peng Liu [b,**], Zhichun Liu [a], Wei Liu [a,*]

[a] School of Energy and Power Engineering, Huazhong University of Science and Technology, Wuhan, 430074, China
[b] Institute of Thermal Science and Power Engineering, Wuhan Institute of Technology, Wuhan, 430205, China

ARTICLE INFO

Keywords:
Parabolic trough receiver
Single conical strip
Multi-objective optimization
Wall temperature uniformity
Actual efficiency

ABSTRACT

Parabolic trough collectors are the crucial component of the concentrated solar power plant, which can meet heat demand and mitigate energy shortages. However, their operation suffers from defects of high local temperature and poor wall temperature uniformity. To alleviate this issue, an enhanced parabolic trough receiver (PTR) with a novel single conical strip insert is proposed and numerically investigated in detail. Furthermore, the effects of structural parameters of the conical strip on the enhanced PTR are investigated, and multi-objective optimization is conducted to determine the optimal parameters. Finally, the performance of the optimal enhanced PTR is evaluated under different operating conditions. The results show two symmetrical longitudinal vortices are formed in the absorber tube due to the guidance of the conical strip, which is beneficial to enhancing fluid mixing and heat transfer. Accordingly, the temperature uniformity of the absorber tube and the actual efficiency are effectively improved. Compared to the smooth PTR, the tube wall temperature is dropped by up to 168 K, and the actual efficiency is improved by 3.3% at most. Moreover, the entropy generation and exergy destruction are reduced by 22.2%–49.3% and 30.6%–45.9%, respectively. This research may guide designing the PTR for efficient and safe operation.

1. Introduction

Solar energy is an abundant renewable energy source, which has great potential for alleviating global energy shortages and environmental problems. Concentrating solar power (CSP) technologies have been widely developed for large-scale thermal utilization of solar energy [1]. Among them, the parabolic trough receiver (PTR), which consists of a parabolic trough reflector and an evacuated receiver, is one of the most mature techniques for commercial use [2], as shown in Fig. 1. In the PTR, solar rays are reflected by the reflector and concentrated on the absorber tube, following which they are subsequently absorbed by the fluid inside the tube. However, due to the unique concentrating characteristics of the reflector, the absorber tube is subjected to a highly non-uniform heat flux which will induce a high circumferential temperature gradient as well as a high local temperature region in the absorber tube. On the one hand, the high temperature gradient causes a large thermal strain in the absorber tube, which in turn leads to bending of the absorber tube or even damage to the outer glass tube [3]. On the other hand, the performance of the selective coating gradually degrades with the increase of the local temperature, thereby the radiative heat loss will gradually increase, leading to the reduction of the overall system efficiency [4]. Enhancing the heat transfer between the heat transfer fluid (HTF) and the absorber tube can ease the temperature gradient in the absorber tube and improve the thermal performance of the PTR. Therefore, it is a potentially feasible method to solve the above problems. In recent years, research on technologies of heat transfer enhancement for PTRs has drawn extensive attention and aroused research interest.

Using nanofluid, improving the tube structure, and applying inserts are the three most prominent methods of heat transfer enhancement technologies for PTRs [5]. The nanoparticles commonly used in HTF include Cu, Au, Ag, Fe_2O_3, Al_2O_3, ZnO, TiO_2, CuO, SiO_2, etc [6,7]. Panduro et al. introduced different nanofluids as the HTF for PTRs and identified the main obstacles to the large-scale applications of nanofluids [8]. Besides the nanofluids, plentiful structural improvement techniques have been developed for improving the thermal performance of PTRs, such as fins (e.g. helical fins and longitudinal fins), unilateral longitudinal vortex generators, dimpled tubes, corrugated tubes,

* Corresponding author.
** Corresponding author.
E-mail addresses: peng_liu@hust.edu.cn (P. Liu), w_liu@hust.edu.cn (W. Liu).

https://doi.org/10.1016/j.renene.2022.08.131
Received 22 April 2022; Received in revised form 5 August 2022; Accepted 26 August 2022
Available online 7 September 2022
0960-1481/© 2022 Published by Elsevier Ltd.

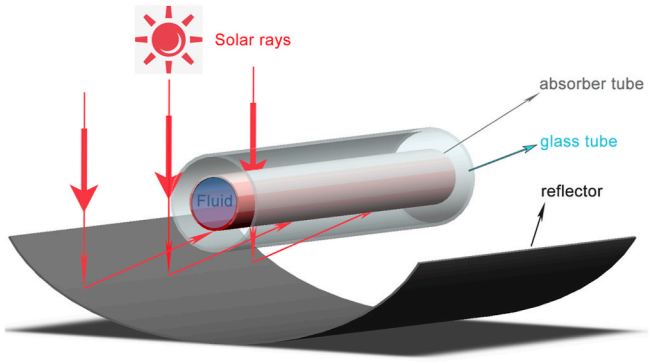

Fig. 1. A diagram of the PTR for solar collection.

sinusoidal tubes, etc [9,10]. As structural improvement techniques require more sophisticated processing technology, inserts, which are low-cost and easy to install, are favored in comparison. Various inserts, such as tape inserts (e.g. wavy tape [11], helical screw-tape [12], wall-detached twisted tape [13], and louvered twisted tape [14]), perforated plates [15], porous inserts (e.g. porous media [16] and porous discs [17]), wire coils (e.g. triangle cross-sectioned wire coil [18] and helical coil [19]), rings (e.g. toroidal ring [20] and perforated ring [21]), conical inserts [22], etc, were designed for the absorber tube due to their abilities to effectively disturb the flow field so as to increase the thermal performance of PTRs. Mwesigye et al. [13] investigated the thermal performance of an enhanced PTR with wall-detached twisted tape inserts through numerical simulations and pointed out that the entropy generation of the enhanced PTR was reduced by up to 58% compared to the smooth PTR. Jamal-Abad et al. [16] experimentally investigated the thermal performance of an absorber tube filled with copper foam, and the results showed that the Nusselt number increases accompanied by a significant increase in the friction factor. Yılmaz et al. [18] numerically simulated the PTR inserted with a wire coil and discovered that the coil improved the thermal performance of the PTR by promoting fluid mixing and disrupting the thermal boundary layer. Ahmed et al. [20] investigated the performance of toroidal rings in PTR and found a maximum thermal efficiency improvement of 3.74%. Mohammed et al. [22] conducted a numerical study of the PTR with conical inserts under turbulent flow conditions. The results showed that the thermal performance of the enhanced tube was significantly improved, and the maximum reduction in entropy generation rate was 42.7%.

Conical strips excel in terms of thermal-hydraulic performance among the various inserts. The conical strip inserted in the circular tube to enhance heat transfer under turbulent conditions was firstly proposed by Fan et al. [23]. The results showed that the conical strips had a good enhancement in heat transfer with PEC values ranging from 1.67 to 2.06. Deshmukh et al. [24] experimentally investigated the heat transfer and pressure drop characteristics of a circular tube equipped with a conical strip. They used air as the working fluid and observed that the average heat transfer characteristics of the conical strip were better than the conventional helical wire coil. Liu et al. [25] developed a principle of convective heat transfer enhancement based on exergy destruction minimization. They proved that multi-longitudinal swirls flow is the best flow field for balancing heat transfer and flow resistance and observed multi-longitudinal swirls in the tube inserted with the conical strip by simulation and experiment. Pourramezan et al. [26]. numerically analyzed the heat transfer process in a circular tube equipped with the twisted conical strip and suggested the realizable k-ε model for more reliable results under turbulent flow conditions with high Reynolds numbers. Kutbudeen et al. [27] examined the performance of the staggered and non-staggered conical strips in PTRs and analyzed that the vortex caused by the conical strips was the main reason for the increase in heat transfer and flow resistance. Liu et al. [28] provided entropy and exergy analysis for PTRs with the conical strip based on the second law of thermodynamics. The maximum reduction of entropy generation by 74.2% and the maximum improvement of the exergy efficiency by 5.7% were achieved due to the double conical strip. Bahiraei et al. [29] experimented on a circular tube equipped with the twisted conical strip and investigated the effect of different twist angles and pitch ratios on its thermal performance. It was found that the heat transfer performance and pressure drop decreased with decreasing twist angles and pitch ratios. They also developed an optimized design for the geometric parameters of the twisted conical strip in another work [30]. Abed et al. [31] investigated and compared the effect of various inserts on the performance of PTRs. The results found that the absorber tube with a large conical strip has lower heat loss compared to other structures.

Although enhancing the heat transfer between the HTF and the absorber tube can improve the temperature uniformity of the absorber tube and increase the heat-collecting efficiency of PTRs, the enhanced heat transfer always comes at the penalty of a significant increase in flow resistance. In other words, the increased pressure loss will lead to more pumping power consumption of the system, which may reduce the operation economy of PTRs. Therefore, how to balance the benefits of enhanced heat transfer and the penalty of increased flow resistance has become one of the main issues of research. Some researchers have provided promising approaches to solve the above problem by applying multi-objective optimization methods to heat transfer enhancement techniques [32–35].

Due to the structure characteristics of PTRs, the lower half part of the absorber tube is subjected to extremely high heat flux while the upper half part only bears little heat flux. Therefore, enhancing the local convective heat transfer rate near the wall of the lower part of the absorber is the main focus. A review of the literature reveals that most of the previous studies on conical strips have focused on the overall heat transfer performance of the fluid in the tube without adapting the configuration to the boundary conditions of particular applications. The local convective heat transfer coefficient needs to be enhanced in the high heat flux region, while the low flux region can be ignored to avoid unnecessary pressure drop losses. To this end, a novel single conical strip insert with a downward sloping arrangement is proposed to enhance the heat transfer of the PTR in this study. This novel single conical strip is expected to guide the fluid to impinge the inner wall of the lower half of the absorber tube. As a result, the high local heat transfer coefficient at the high heat flux region is expected to be achieved. In addition, multi-longitudinal swirls are expected to be formed in the absorber tube to balance the heat transfer and flow resistance. To analyze the flow and heat transfer characteristics of the enhanced PTR fitted with the single conical strip insert and to evaluate its performance advantages over a smooth PTR, comprehensive numerical simulations of the enhanced PTR and the smooth PTR are conducted in this paper. Moreover, the influence of different parameters of the conical strip on the thermal-hydraulic performance of the PTR is analyzed, and the optimal conical strip parameters are obtained by a multi-objective optimization algorithm to improve the overall performance. Finally, the performance of the optimal combination of parameters is evaluated under different operating conditions, including various mass flow rates (M), inlet temperatures (T_{inlet}), and direct solar irradiances (DNI). This research may provide some practical guidance for designing more efficient and safe PTRs.

Table 1
Main structural parameters of SEGS LS-2 [36].

Structural parameter	Value
Overall length of absorber tubes L/m	7.8
Inner diameter of absorber tubes d_{ri}/mm	66
Outer diameter of absorber tubes d_{ro}/mm	70
Inner diameter of glass tubes d_{gi}/mm	109
Outer diameter of glass tubes d_{go}/mm	115

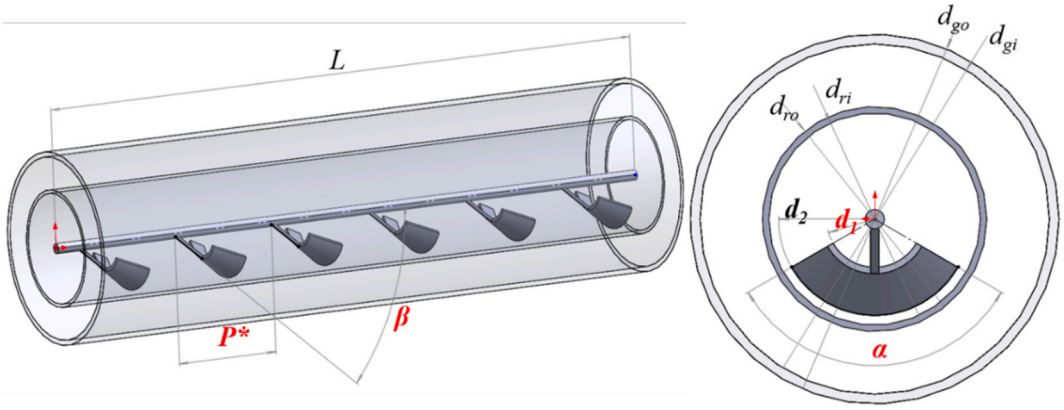

Fig. 2. A physical model schematic of the PTR with a single conical strip insert.

2. Physical model

The research objective in this study is the SEGS LS-2 solar collector, whose main structural parameters are listed in Table 1 [36]. There are four calculation zones in the PTR, namely, the HTF zone, the solid zone of the absorber tube, the vacuum zone between the absorber tube and the glass tube, and the solid zone of the glass tube. The heat transfer between zones is realized through the interfaces. A physical model schematic of the PTR with a single conical strip insert is shown in Fig. 2. The conical strip is sliced from a hollow cone of diameter $d_2 = 60$ mm and fixed to a circular rod with a diameter of 6 mm. The main parameters of the conical strip are inner diameters (d_1), central angles (α), inclined angles (β), and pitch ratios ($p = p^*/d_{ri}$), whose effects on the thermal performance of the PTR are investigated in this paper.

3. Simulation method

The essential assumptions in this model are given as follows.

(1) The process of flow and heat transfer is a steady state.
(2) The absorber tube and the conical strip are rigid bodies, and their deformation and vibration are not considered.
(3) The walls of the absorber tube and the conical strip are no-slip surfaces.
(4) The heat conduction of the conical strip is not considered.
(5) The working fluid is a continuous, incompressible, and isotropic Newtonian fluid.
(6) The effect of gravity and viscous heating is neglected.*3.1 Governing equations*

The Reynolds numbers studied in this paper are all bigger than 5000, thus the flow has been developed into a turbulent regime. The realizable k-ε turbulence model is used in this numerical model for its high precision in calculating turbulent flows such as cyclones and vortices [37]. Thus, the governing equations are expressed as follows [38]:

Continuity equation:

$$\frac{\partial(\rho u_i)}{\partial x_i} = 0 \tag{1}$$

Momentum equation:

$$\frac{\partial(\rho u_i u_j)}{\partial x_i} = -\frac{\partial P}{\partial x_i} + \frac{\partial}{\partial x_j}\left((\mu+\mu_t)\left(\frac{\partial u_i}{\partial x_j}+\frac{\partial u_j}{\partial x_i}\right) - \frac{2}{3}(\mu+\mu_t)\frac{\partial u_i}{\partial x_i}\delta_{ij} - \rho\overline{u_i' u_j'}\right) \tag{2}$$

Energy equation:

$$\frac{\partial(\rho u_i T)}{\partial x_i} = \frac{\partial}{\partial x_i}\left(\frac{\mu}{\mathrm{Pr}}+\frac{\mu_t}{\mathrm{Pr}_t}\right)\frac{\partial T}{\partial x_i} \tag{3}$$

Kinetic energy (k) equation:

$$\frac{\partial(\rho u_i k)}{\partial x_i} = \frac{\partial}{\partial x_i}\left(\left(\mu+\frac{\mu_t}{\sigma_k}\right)\frac{\partial k}{\partial x_i}\right) + \Gamma - \rho\varepsilon \tag{4}$$

Dissipation rate (ε) equation:

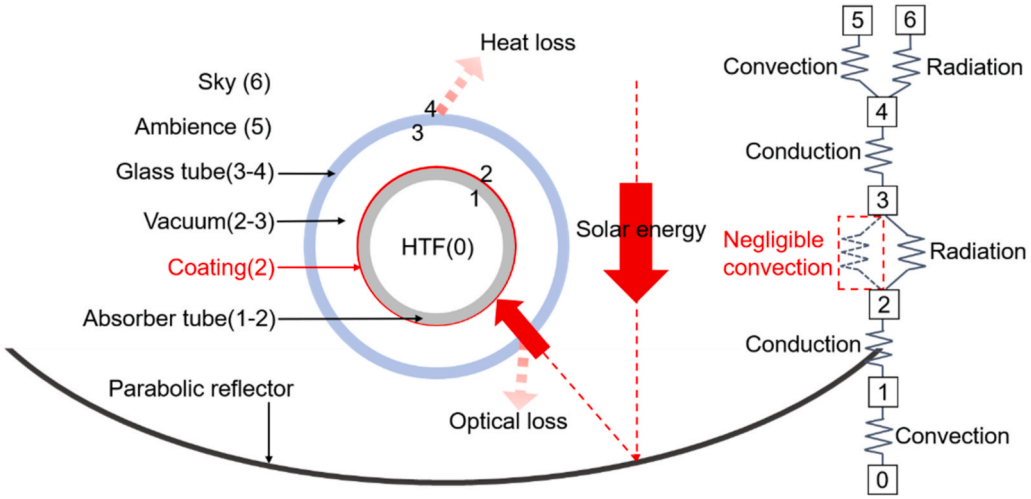

Fig. 3. Calculation model thermal resistance network.

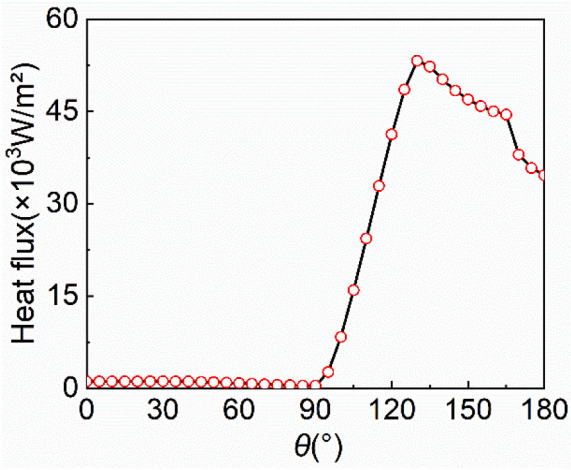

Fig. 4. Circumferential heat flux distribution of the absorber tube [39].

Table 2
Physical properties of Syltherm 800 [40].

Physical properties	$a+b\times T+c\times T^2+d\times T^3+e\times T^4$				
	a	b	c	d	e
ρ, kg/m^3	1.106×10^{3}	-4.154×10^{-1}	-6.062×10^{-4}		
λ, W/(m·K)	1.900×10^{-1}	-1.875×10^{-4}	-5.753×10^{-10}		
C_p, J/(kg·K)	1.108×10^{3}	1.708			
μ, Pa·s	8.487×10^{-2}	-5.541×10^{-4}	1.388×10^{-6}	-1.566×10^{-9}	6.672×10^{-13}

$$\frac{\partial(\rho u_i \varepsilon)}{\partial x_i}=\frac{\partial}{\partial x_i}\left(\left(\mu+\frac{\mu_t}{\sigma_\varepsilon}\right)\frac{\partial \varepsilon}{\partial x_i}\right)+c_1\Gamma\varepsilon-\rho c_2\frac{\varepsilon^2}{k+\sqrt{v\varepsilon}} \tag{5}$$

The turbulent kinetic energy (Γ) in Eq. (5) is defined as:

$$\Gamma=-\overline{u_i u_j}\frac{\partial u_i}{\partial x_i}=\mu_t\left(\frac{\partial u_i}{\partial x_j}+\frac{\partial u_j}{\partial x_i}\right)\frac{\partial u_i}{\partial x_i} \tag{6}$$

where ρ, u, P, T, μ, and Pr represent density, velocity, pressure, temperature, dynamic viscosity, and Prandtl number of the fluid, respectively. μ_t and Pr_t represent the turbulent viscosity and the turbulent Prandtl number, respectively. σ_k and σ_ε represent the Prandtl number corresponding to k and ε, respectively.

The governing equations are solved using ANSYS Fluent based on the finite volume method. The SIMPLE algorithm is applied to handle the coupling of velocity and pressure, the governing equations for momentum and energy are discretized with a second-order upwind scheme. Besides, the enhanced wall function is used in the turbulence model. The convergence criteria in this study are: the relative residuals are decreased to 10^{-4} for continuity equation, 10^{-7} for energy equation, and 10^{-5} for other equations.

3.1. Boundary conditions and solution settings

The heat transfer process in this model is the coupling of conduction, convection, and radiation, and the calculation model thermal resistance network is shown in Fig. 3. The non-uniform distribution of heat flux (DNI = 1000 W/m^2) on the outer surface of the absorber tube, which is calculated using Monte Carlo ray tracing (MCRT) by He et al. [39], is applied to the present model as shown in Fig. 4. Most of the heat energy is carried inward by conduction and convection and finally absorbed by the HTF. In addition, the convection loss is negligible due to the near-vacuum environment between the absorber tube and the glass tube. A small amount of heat energy is transferred outward to the glass tube only through radiation and then dissipated to ambiance and sky through convection and radiation on the outer surface of the glass tube.

Syltherm 800 is selected as the HTF in this study, and stainless steel (321H) and Plexiglas are adopted as the materials for the absorber tube and the glass tube, respectively. The thermal conductivities of 321H and Plexiglas are 25 W/(m·K) and 1.2 W/(m·K), respectively. The physical properties of Syltherm 800 are temperature-dependent, and the fitted formulas are listed in Table 2 [36].

The coating on the outer surface of the absorber tube is made of cermet material, and the variation of its emissivity (ε_c) with temperature is described in the following formula:

$$\varepsilon_c=0.000327T_c-0.065971 \tag{7}$$

where T_c represents the outer surface temperature of the absorber tube.

The outer surface of the glass tube is under a mixed convective and radiative boundary condition, and the glass tube is assumed to be a gray body with an emissivity of 0.86. The ambient temperature is set to 298 K, while the sky temperature is set to 8 K below the ambient [41]. The convective heat transfer coefficient (h_w) between the glass tube and the ambient is determined by the following formula [42]:

$$h_w=4{u_0}^{0.58}d_{go}^{-0.42} \tag{8}$$

where u_0 represents the ambient wind speed which is taken as 2.5 m/s in this study, and d_{go} represents the outer diameter of the glass tube.

3.2. Parameter definitions

This subsection will focus on the main parameters involved in this study, including basic parameters and performance parameters describing the thermal performance of the system. Reynolds number (Re), maximum wall temperature difference (ΔT_w), heat transfer factor (h), friction factor (f), and mean Nusselt number (Nu) are defined as follows.

$$\mathrm{Re}=\frac{\rho u_{\mathrm{in}}\ d_{ri}}{\mu} \tag{9}$$

$$\Delta T_w=T_{w\max}-T_{w\min} \tag{10}$$

$$h=\frac{q_{eff}}{\left(T_{\mathrm{w}}-T_f\right)} \tag{11}$$

$$f=\frac{2\Delta P d_{ri}}{\rho u_{\mathrm{in}}^2\ L} \tag{12}$$

$$Nu=\frac{hd_{ri}}{\lambda} \tag{13}$$

where u_{in} represents the mean velocity of the fluid at the inlet of the absorber tube. ρ, μ, and λ represent the density, dynamic viscosity, and thermal conductivity of the fluid at a temperature of T_f, respectively. T_w, T_{wmax}, and T_{wmin} represent the mean temperature at the inner wall of the absorber tube, and the maximum and minimum temperature of the absorber tube, respectively. q_{eff} represents the mean heat flux at the inner wall of the absorber tube, and ΔP represents the pressure drop between the inlet and outlet of the absorber tube.

To better analyze the heat transfer performance along the circumferential direction of the PTR, the mean circumferential temperature (T_{cir}), the circumferential heat flow flux (q_{cir}), and the circumferential Nusselt number (Nu_{cir}) at the inner surface of the absorber tube are defined as follows.

$$T_{\mathrm{cir}}=\frac{1}{L\Delta\theta}\int_0^L\int_{\theta_i}^{\theta_i+\Delta\theta}T_w d\theta dx \tag{14}$$

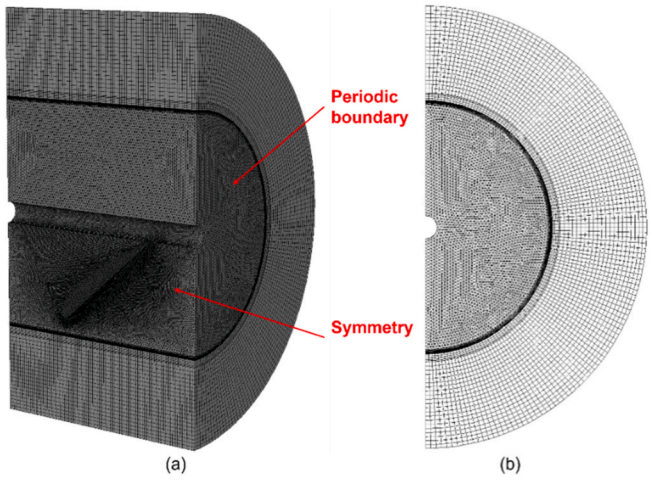

Fig. 5. Three-dimensional grid model: (a) lateral view; (b) cross section view.

$$q_{\mathrm{cir}} = \frac{1}{L\Delta\theta}\int_0^L \int_{\theta_i}^{\theta_i+\Delta\theta} q d\theta dx \tag{15}$$

$$Nu_{\mathrm{cir}} = \frac{1}{L\Delta\theta}\int_0^L \int_{\theta_i}^{\theta_i+\Delta\theta} Nu d\theta dx \tag{16}$$

The entropy generation and exergy destruction are employed to evaluate the irreversibility of the PTR, where the total entropy generation per unit volume of fluid (S_{gen}) can be divided into the flow entropy generation from flow resistance irreversibility and the heat transfer entropy generation from heat transfer irreversibility, and similarly, the total exergy destruction per unit volume of fluid (E_{xd}) consists of the flow exergy destruction caused by fluid pressure drop and the heat transfer exergy destruction caused by heat transfer temperature difference.

$$S_{\mathrm{gen}} = \frac{1}{V}\iiint_{\Omega}\left[\frac{\mu}{T}\left(\frac{\partial u_i}{\partial x_j}+\frac{\partial u_j}{\partial x_i}\right)\frac{\partial u_i}{\partial x_j}+\frac{\rho\varepsilon}{T}\right]dV + \frac{1}{V}\iiint_{\Omega}\left[\left(1+\frac{a_t}{a}\right)\frac{\lambda}{T^2}(\nabla T)^2\right]dV \tag{17}$$

$$E_{xd} = \frac{1}{V}\iiint_{\Omega} u\cdot(\rho u\cdot\nabla u-\mu\nabla^2 u)dV + \frac{1}{V}\iiint_{\Omega} T_0\frac{\lambda(\nabla T)^2}{T^2}dV \tag{18}$$

where ∇T and a represent the temperature gradient and the thermal diffusivity of the fluid at a certain location, respectively. V represents fluid volume and T_0 represents the ambient temperature.

In engineering practice, it is also necessary to consider the pump power consumption, heat loss, and total efficiency during the operation of the PTR. Therefore, the pump power consumption (W_p) and the actual efficiency (η) of the PTR are also defined in this study as follows:

$$Q_{loss} = Q_{solar} - Q_{eff} = DNI\cdot A - \frac{\pi d_{ri}}{4}q_{eff} \tag{19}$$

$$W_p = \frac{\pi d_{ri}^2}{4}u_{in}\Delta P \tag{20}$$

$$\eta = \frac{Q_{eff} - W_p/\eta_e}{Q_{solar}} \tag{21}$$

where Q_{solar}, Q_{eff}, and Q_{loss} respectively represent the total solar radiation input to the PTR, the heat absorbed by the HTF, and the heat loss. DNI represents the direct normal irradiance. A represents the area of the parabolic reflector zone which is specified as $5\times7.8\ \mathrm{m}^2$ η_e represents the power generation efficiency which is taken as 0.33 in this study [43].

Table 3
Grid independence verification.

Grid number	*Nu*	Error	*f*	Error	T_{wmax}	Error
777310	246.36	1.37%	0.3623	3.49%	605.27	0.26%
1634566	243.78	0.30%	0.3541	1.15%	606.73	0.01%
2580060	243.33	0.12%	0.3510	0.25%	607.31	0.08%
3514725	243.04	–	0.3501	–	606.82	–

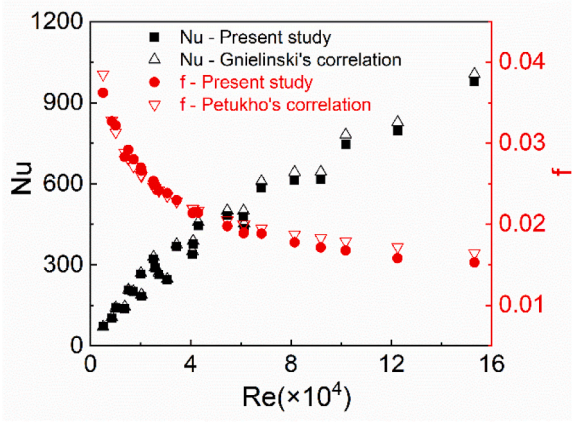

Fig. 6. Comparisons of correlations and simulation results.

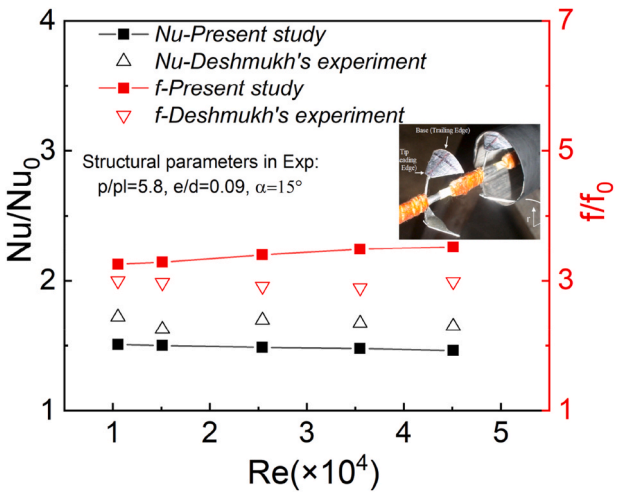

Fig. 7. Comparisons of numerical and experimental results.

3.3. Mesh independence test

Considering the symmetry of the physical model, only one pitch unit along the flow direction and half of the physical model is taken in the computational model to save computational resources, thus the symmetric and periodic boundary settings are used. Gambit is used to establish a three-dimensional grid model, which is shown in Fig. 5. A highly dense grid is used in the boundary layer of the inner wall of the absorber tube to ensure $y^+<1$. To eliminate the influence of grid number on the calculation results, a grid independence verification of the enhanced PTR inserted with a single conical strip is carried out. The calculation conditions are taken as $M = 0.57$ kg/s, $T_{inlet} = 500$ K, and $DNI = 1000\ \mathrm{W/m^2}$. The parameters of the conical strip are $d_1 = 30$ mm, $\alpha = 75^\circ$, $\beta = 50^\circ$, and $p = 1$, the verification results are listed in Table 3.

Table 4
Validation between simulation and experimental data.

Case	1	2	3	4	5	6	7	8
DNI (W/m^2)	933.7	968.2	982.3	909.5	937.9	880.6	920.9	903.2
Wind speed (m/s)	2.6	3.7	2.5	3.3	1	2.9	2.6	4.2
Air temperature (K)	294.4	295.6	297.5	299.4	302	300.7	302.7	304.3
Flow rate (kg/s)	0.6872	0.6534	0.6350	0.6580	0.6206	0.6205	0.5457	0.5673
T_{inlet} (K)	375.4	424.2	470.7	523.9	571	572.2	652.7	629.1
ΔT (K) (Exp)	21.8	22.02	21.26	18.7	19.1	18.2	18.1	18.5
ΔT (K) (Sim)	21.49	22.3	22.13	18.57	19.09	17.85	18.54	18.28
ΔT error (%)	1.4	1.29	4.1	0.68	0.06	1.95	2.43	1.21
Efficiency (Exp)	72.51	70.9	70.17	70.25	67.98	68.92	62.34	63.83
Efficiency (Sim)	70.94	70.71	70.13	69	67.49	67.23	62.61	64.25
Efficiency error (%)	2.16	0.26	0.06	1.77	0.72	2.45	0.43	0.67

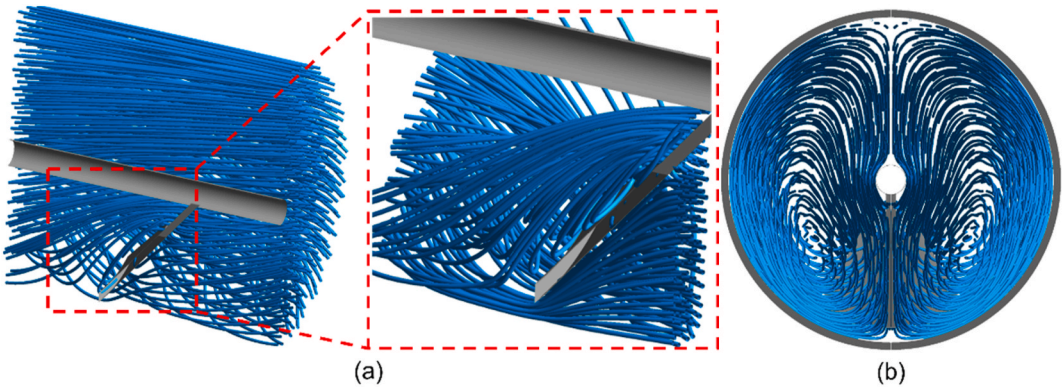

Fig. 8. Streamlines in the absorber tube of enhanced PTR: (a) lateral view; (b) cross section view.

3.4. Model validation

Gnielinski's correlation [44] and Petukhov's correlation [45], which are given by Eqs. (22) and (23), are applied to verify the accuracy of the model for simulating heat transfer performance (Nusselt number) and flow resistance (friction factor), respectively. The multiplier $(Pr_f/Pr_w)^{0.11}$ is used for friction factor correction due to variations of properties [46]. The average deviations of *Nu* number and *f* are 3.48% and 2.80%, and the maximum deviations are 4.65% and 8.21%, as shown in Fig. 6, which shows the results from numerical simulation and the correlations are in good agreement. Fig. 7 presents comparisons of the simulation with experimental results for similar conical inserts [24]. The maximum deviations of the Nusselt number ratio and the friction factor ratio were 12.51% and 20.62%, respectively. Due to unavoidable differences between simulations and experiments, such as differences in working fluid properties and boundary conditions, and uncertainties in experimental measurements, the numerical model has reasonable accuracy. In addition, the present numerical model is validated by comparison with the experimental results of Dudley et al. [36]. The conditions and configurations of experiments chosen from Dudley's work and those of the present numerical model are essentially the same. The comparisons of the inlet-outlet temperature difference and the heat collection efficiency between the numerical model and the experimental works are shown in Table 4. It is found that the numerical results are in good consistent with the experimental data, as the deviations of the inlet-outlet temperature difference and heat collection efficiency are within 4.10% and 2.45%, respectively.

$$Nu_G = \frac{(f/8)(Re-1000)\mathrm{Pr}_f}{1+12.7(f/8)^{0.5}\left(\mathrm{Pr}_f{}^{2/3}-1\right)}\left[1+\left(\frac{d_{ri}}{L}\right)^{2/3}\right] \tag{22}$$

$$f_P = [1.82\lg(Re)-1.64]^{-2} \tag{23}$$

4. Results and discussion

4.1. Heat transfer enhancement mechanism

In this subsection, the heat transfer enhancement mechanism will be analyzed from the flow field and temperature distribution, respectively. The case of the enhanced PTR with geometric parameters being $d_1 = 24$ mm, $\alpha = 60^\circ$, $\beta = 50^\circ$, and $p = 1$ is selected to conduct analysis when $M = 0.57$ kg/s, $T_{inlet} = 500$ K, and $DNI = 1000$ W/m^2.

Fig. 8 gives the streamlines in the absorber tube of the enhanced PTR with the conical strip. As seen in Fig. 8 (a), the upstream part of the fluid flowing through the conical strip will be divided into two parts. The upper part of the flow near the central connecting rod will bypass the cone from above and then deflect, while the part of the fluid near the lower tube wall will be guided by the conical strip to scour the tube wall below, which makes sufficient mixing of the fluid in the core region and the boundary layer near the tube wall. Thereafter, the two parts of fluid drive the adjacent fluid to form a whirling forward flow of the whole flow field. As seen in Fig. 8 (b), a pair of vortexes is formed on both sides of the conical strip from the mainstream direction, confirming the previous analysis that the fluid will spiral forward. In addition, the fluid disturbance near the lower half part of the absorber tube, where the wall suffers the extremely high heat flux, is apparently stronger than that of the upper half part of the absorber tube. This is consistent with our expectation of strengthening the local heat transfer coefficient of the fluid with the higher heat flux zone.

Fig. 9 (a) displays the temperature distribution of the absorber tube for the enhanced PTR and the smooth PTR. The conical strip guides the fluid to scour the high heat flux zone on the lower surface of the absorber tube, which strengthens the local heat transfer coefficient between the fluid and the inner wall of the absorber tube. As a result, the overall temperature of the inner wall considerably reduces, with the peak temperature dropping from 683K to 518K, as shown in Fig. 9 (a). Fig. 9 (b) presents the circumferential temperature of the tube wall and

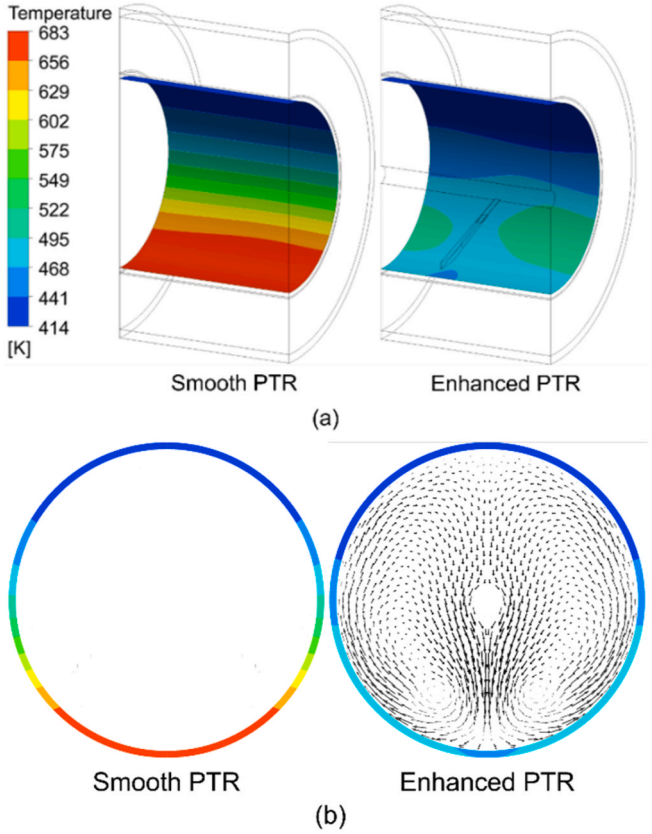

Fig. 9. Flow field and temperature distributions of the enhanced PTR and smooth PTR: (a) temperature distribution of the inner wall; (b) circumferential wall temperature and tangential velocity distributions in the cross-section downstream of the conical strip.

tangential velocity distributions in the cross-section downstream of the conical strip in the enhanced PTR and the same position in the smooth PTR. The tangential velocity distribution shows the formation of a pair of vortexes in the tube, which is consistent with the results of the streamline analysis in Fig. 8. The development of tangential velocities allows the cold fluid in the core zone of the tube to be pushed to the high heat flux zone of the tube wall, thus achieving higher local heat transfer performance. The fluid with high temperature in the lower part of the absorber tube then flows along the direction of the vortexes back to the core zone. Therefore, the fluids in the core zone and boundary layer are fully mixed, thus improving the temperature uniformity of the absorber tube and reducing the circumferential temperature difference.

Fig. 10 displays the trends of circumferential heat flux, circumferential temperature, and circumferential *Nu* number with circumferential angle (θ) in the inner wall of the absorber tube. The heat transfer capacity is greatly enhanced due to the continuous scouring of the fluid to the wall by the conical strip, so the local heat flux in the region with θ ranging from 120° to 180° of the enhanced PTR is obviously increased when compared to that of the smooth PTR, as shown in Fig. 10 (a). In Fig. 10 (b), it is observed that the circumferential temperature of the enhanced PTR is significantly lower than that of the smooth PTR owing to the scouring effect. In addition, it can be seen from Fig. 10 (c) that the circumferential *Nu* number of the enhanced PTR is slightly smaller than that of the smooth PTR as θ ranges from 0° to 90°. The reason for this phenomenon is that a reverse flow in the area near the upper half of the surface, and the synergistic effect of the flow and temperature fields is weakened. The circumferential *Nu* number of the enhanced PTR is much larger than that of the smooth PTR as θ ranges from 135° to 180°. The average *Nu* number of the enhanced PTR is 2.4 times larger than that of the smooth PTR, which indicates that the conical strip can effectively improve the heat transfer performance between the fluid and the absorber tube.

4.2. Variation of conical strip parameters

Fig. 11 presents the effect of the pitch ratios (p) on the performance of the enhanced PTR under different inclined angles (β) when$\alpha = 30°$, $d_1 = 18$ mm, $Re = 5000$, $T_{inlet} = 500$ K, and $DNI = 1000$ W/m^2. It can be observed that the Nu/Nu_0 gradually decreases with the increase of p, as shown in Fig. 11 (a). The reason is that p represents the placement distance of the conical strip, which mainly affects the scouring frequency of the fluid on the wall. The higher the scouring frequency, the stronger the heat transfer capability. Besides, with the increase of β, Nu/Nu_0 increases initially and then starts to drop. When β becomes larger, the fluid will scour the absorber tube wall with a larger angle, which is closer to 90°. As a result, the scouring intensity of the fluid on the wall is enhanced and thus the heat transfer is improved. However, when the $\beta > 45°$, some of the fluid flows around the strip on both sides, and less fluid is directed towards the tube wall. Thus, the heat transfer performance decreases slightly as the β increases. As p decreases and β increases, f/f_0 gradually increases as described in Fig. 11 (b). Fig. 11 (c) shows that the overall performance (PEC value) is larger than 1, which means that the benefit of heat transfer enhancement is greater than the cost of flow resistance increase. In addition, the better overall performance of the enhanced PTR is obtained at the small p and β. In Fig. 11 (d), (T_{wmax}-$T_{wmax,0}$) represents the difference between the peak temperature of the absorber tube for the enhanced PTR and the smooth PTR. The variation of (T_{wmax}-$T_{wmax,0}$) ranges from 134 K to 158 K, illustrating that the conical strip effectively reduces the peak temperature of the tube wall.

Fig. 12 presents the effects of the central angles (α) and inner

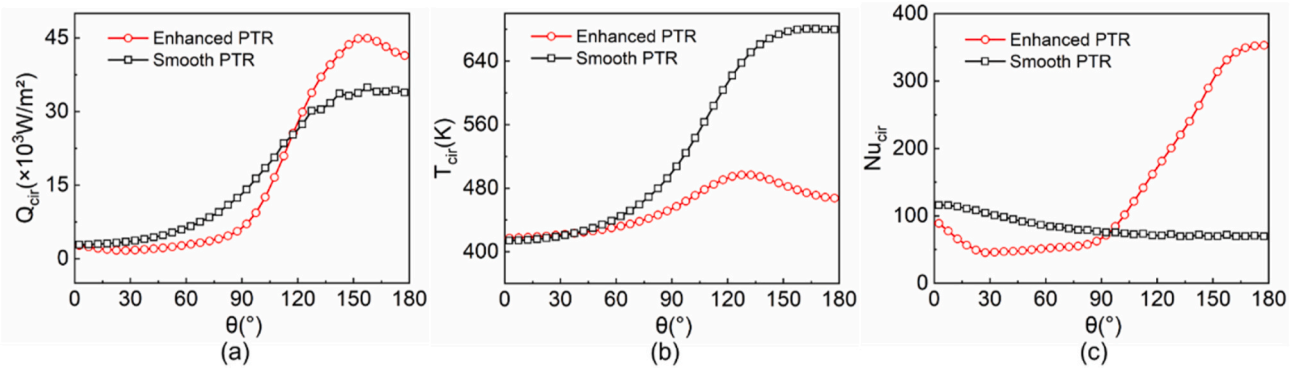

Fig. 10. Comparison of circumferential performance variables of the enhanced PTR and the smooth PTR: (a) circumferential heat flux; (b) circumferential temperature; (c) circumferential Nusselt number.

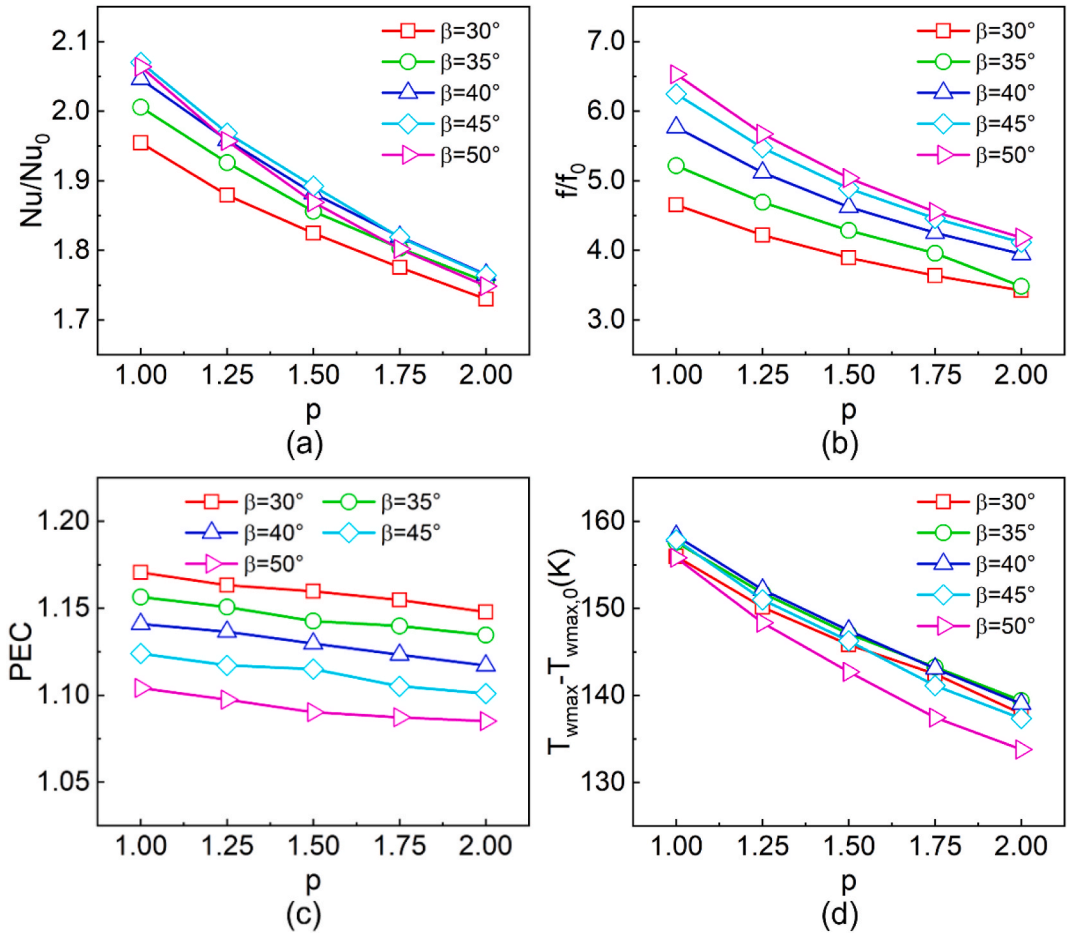

Fig. 11. Performance comparisons of the enhanced PTR with pitch ratios and the smooth PTR for different inclined angles: (a) Nusselt number ratio; (b) friction factor ratio; (c) *PEC*; (d) peak temperature difference.

diameters (d_1) on the performance of the enhanced PTR when $\beta = 40°$, $p = 1.5$, $Re = 5000$, $T_{inlet} = 500$ K, and $DNI = 1000$ W/m^2. The cross-sectional area of the conical strip in the tube increases with the decrease of d_1 and the increase of α. In turn, the disturbance intensity of the conical strip to the fluid is increased, which not only strengthens heat transfer but also causes an increase in flow resistance. Therefore, the Nu/Nu_0 and f/f_0 perform a similar trend in large part, as expected from Fig. 12 (a) and Fig. 12 (b). Moreover, Nu/Nu_0 and f/f_0 vary in the ranges of 1.79–2.30 and 4.00–16.37, respectively. As α increases, the perturbation enhancement effect of the conical strip on the flow field becomes less and less significant, and even the heat transfer capacity is weakened instead in the case of relatively large d_1, as shown in Fig. 12 (a). From Fig. 12 (c), the *PEC* value of the enhanced PTR ranges from 0.90 to 1.13. The effect of d_1 on *PEC* is not obvious, while the *PEC* value decreases progressively with the increasing α. It is because the penalty of excessive pressure drop loss caused by the increasing α covers the benefit of heat transfer enhancement. The drop in overall temperature matches the increase in heat transfer ability, thus the trends of (T_{wmax}-$T_{wmax,0}$) in Fig. 12 (d) are following those of Nu/Nu_0 in Fig. 12 (a). The maximum drop in peak temperature of the enhanced PTR is 173K compared to the smooth PTR.

4.3. Optimization design

As analyzed in the previous subsection, the parameters of the conical strip have a considerable influence on the performance of the enhanced PTR, and different combinations of parameters bring various effects. Considering that there are two conflicting performance objectives (i.e. thermal efficiency and pump power consumption) in the research, the heat loss ratio index and the pump power consumption ratio index, which are defined as Eqs. (24) and (25), are selected as the optimization objectives according to the engineering application background. To get the best balance between thermal efficiency and pump power consumption in the enhanced PTR, multi-objective optimization is conducted to obtain the optimized combination of parameters, and the optimization process is presented in Fig. 13. Firstly, five different values of inner diameters (d_1), central angles (α), inclined angles (β), and pitch ratios (p) are selected, respectively. Secondly, 125($5 \times L_{25}(5^6)$) cases of parameter combinations are calculated by CFD software with the idea of orthogonal experimental design. Thirdly, artificial neural networks (ANN) [47] are employed to train and fit the dataset, and the objective function of input and output is obtained. Fourthly, The non-dominated sorting genetic algorithm (NSGA-II) [48] is applied to optimize the objective function to acquire the Pareto front. Finally, the optimized parameter combinations are determined according to the Technique for the Order Preference by Similarity to Ideal Solution (TOPSIS) [49], and the optimization results are verified by numerical simulation.

$$Objective_1 = HLR = \frac{Q_{loss}}{Q_{loss,0}} \tag{24}$$

$$Objective_2 = PCR = \frac{W_p}{W_{p,0}} \tag{25}$$

Fig. 14 provides a schematic diagram of the ANN structure. ANN contains an input layer with 4 neurons, a hidden layer with several neurons, and an output layer with a neuron. ANN divides the resultant

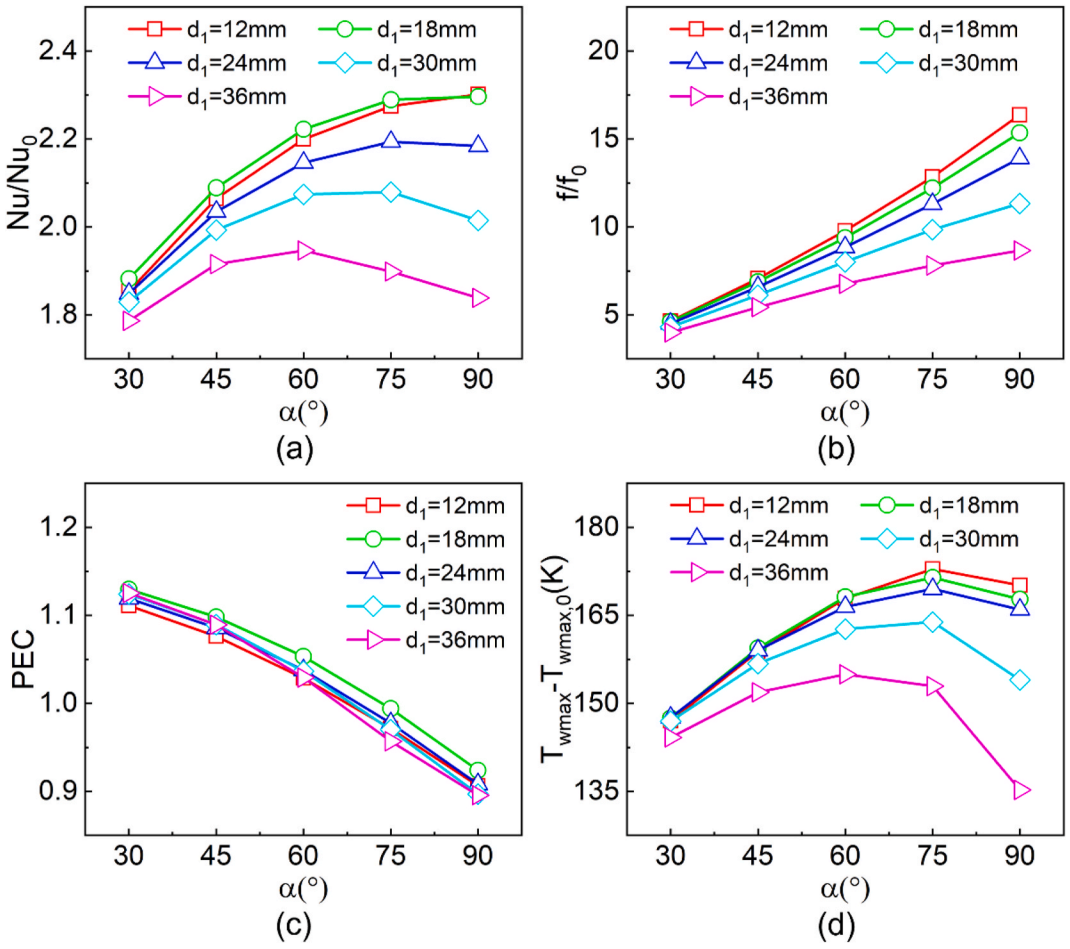

Fig. 12. Performance comparisons of the enhanced PTR with various central angles and the smooth PTR for different inner diameters: (a) Nusselt number ratio; (b) friction factor ratio; (c) *PEC*; (d) peak temperature difference.

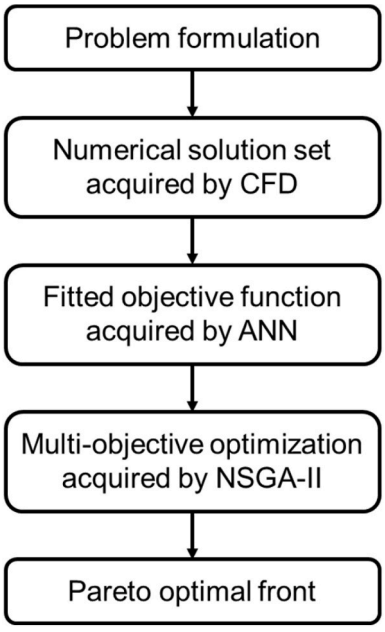

Fig. 13. Flowchart of optimization.

values obtained from numerical calculations into three groups (70%, 15%, and 15%), which are used to train the entire network using the Bayesian-regularization algorithm, verify the generality of the network, and test the network, respectively. The number of neurons in the hidden layer has a significant impact on the prediction accuracy of the whole network. An independence test is carried out to select the optimal number of neurons in the hidden layer. The mean squared error (*MSE*) and regression coefficient (*R*) are selected as the judging criteria, which are defined as:

$$MSE = \frac{1}{n}\sum_{i=1}^{n}\left(X_{i,ANN} - X_i\right)^2 \tag{26}$$

$$R = \sqrt{1 - \sum_{i=1}^{n}\frac{\left(X_{i,ANN} - X_i\right)^2}{X_i^2}} \tag{27}$$

Table 5 lists the training results of ANNs for *HLR* and *PCR* using different numbers of neurons in the hidden layer. The numbers of neurons in the hidden layer of each objective are the same as the ones corresponding to the minimum *MSE* and maximum *R* values. As shown in Table 5, both the optimal numbers of neurons corresponding to *HLR* and *PCR* are 14. To further ensure the accuracy of ANN, the predicted values of ANN and the numerical simulation results are compared and analyzed in this research, and the results are shown in Fig. 15. The predicted values of ANN for *HLR* and *PCR* are in good agreement with the numerical results, and the maximum errors are 1.40% and 2.04%, respectively. Therefore, it is confirmed that objective functions obtained through ANN have reasonable accuracy.

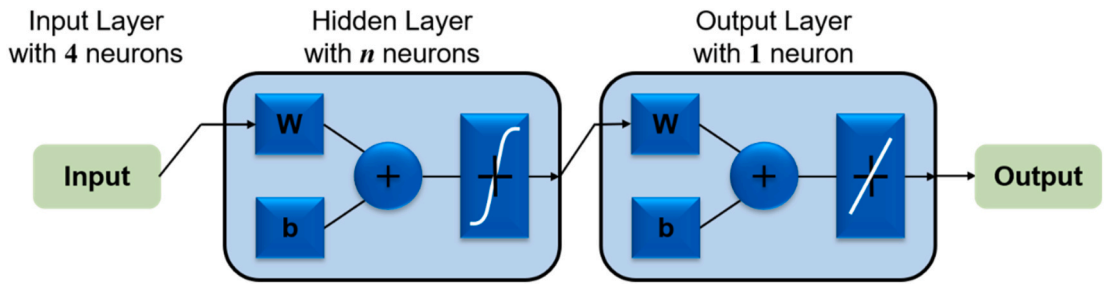

Fig. 14. Structure diagram of the artificial neural network.

Table 5
Neuron independence test for *HLR* and *PCR*.

Number of neurons	$HLR = Q_{loss}/Q_{loss,0}$		$PCR=W_p/W_{p,0}$	
	MSE	R	MSE	R
1	2.94E-04	0.66232	1.3404	0.91077
2	6.38E-05	0.92673	0.4300	0.97137
3	1.27E-05	0.98541	0.2402	0.98401
4	5.20E-06	0.99403	0.0815	0.99458
5	2.01E-06	0.99769	0.0332	0.99779
6	2.44E-06	0.99720	0.0179	0.99881
7	1.66E-06	0.99810	0.0129	0.99914
8	1.37E-06	0.99843	0.0088	0.99941
9	8.78E-04	−0.00791	0.0099	0.99934
10	9.99E-07	0.99885	0.0033	0.99978
11	8.79E-07	0.99899	0.0243	0.99838
12	9.01E-07	0.99897	0.0031	0.99979
13	1.13E-06	0.99870	0.0184	0.99877
14	8.72E-07	0.99900	0.0016	0.99989
15	1.65E-06	0.99810	0.0034	0.99978
16	2.32E-06	0.99734	0.0071	0.99953
17	1.30E-06	0.99851	0.0202	0.99865
18	1.36E-06	0.99844	15.0356	−0.00087
19	1.67E-06	0.99808	0.0043	0.99972
20	1.73E-06	0.99802	0.0109	0.99927

Multi-objective optimization can be described as follows:
Minimization: $f(d_1,\alpha,\beta,p) = \{Q_{loss}/Q_{loss,0}, W_p/W_{p,0}\}$,
Subjected to: $d_1 \in [12,36], \alpha \in [30,90], \beta \in [30,50], p \in [1,2]$.

Variations in the four structural parameters for optimization affect both the mutually opposing *Objective1* and *Objective2*. NSGA-II is used to perform optimization and obtain the Pareto front. The main parameters of NSGA-II selected in this study are listed in Table 6.

Fig. 16 presents the Pareto front obtained by NSGA-II. Each point on the Pareto front is the preferred point, where extreme point A has the

Table 6
Parameter setting of NSGA-II.

Parameter	Value setting
Population size	120
Generation	2000
Crossover fraction	0.8
Pareto factor	0.6
Function tolerance	10^{-5}

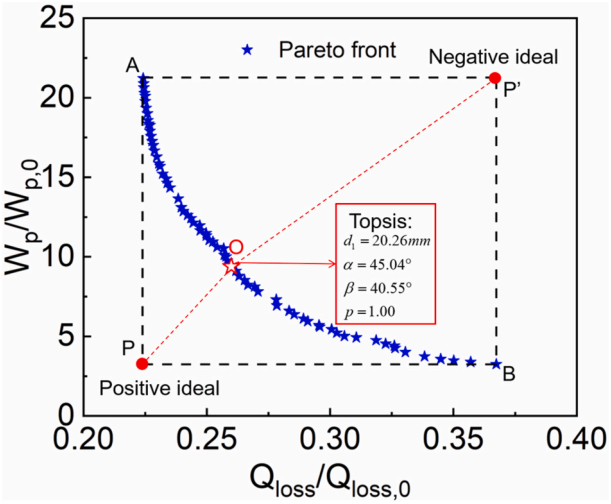

Fig. 16. Pareto front by NSGA-II and optimal point O searched by TOPSIS.

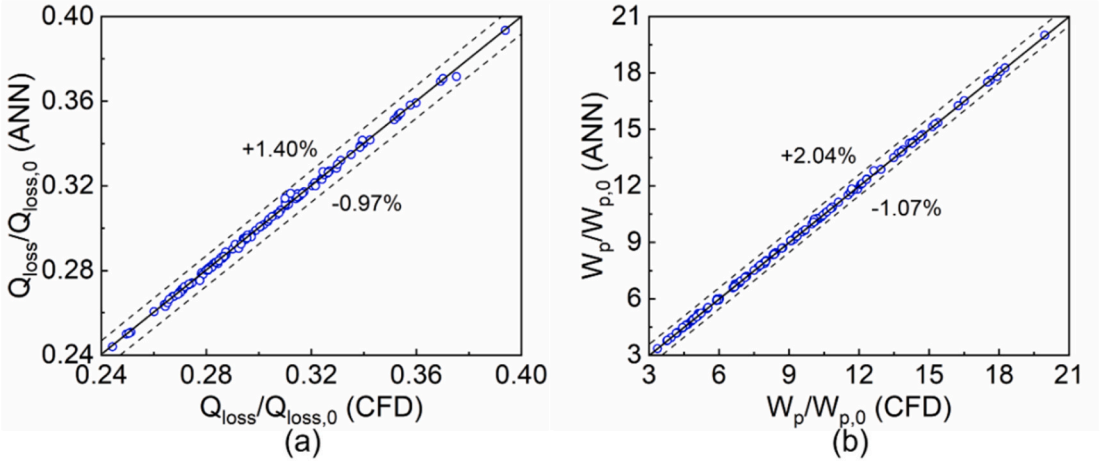

Fig. 15. Comparisons of predicted values by ANN and numerical results: (a) heat loss ratio; (b) pump power consumption ratio.

Table 7
Numerical simulation results of Point A, B, and O.

Point	Nu/Nu_0	f/f_0	PEC	$(T_{wmax}- T_{wmax,0})$
A	2.67	17.87	1.021	173
O	2.31	8.83	1.118	168
B	1.68	3.34	1.123	133

lowest heat loss but the highest pumping power and extreme point B has the lowest pumping power but the highest heat loss. The optimal point O is obtained by reconciling the two conflicting objectives with TOPSIS, which is closest to the positive ideal and farthest from the negative ideal. The CFD calculations indicate that the *Nu* number is decreased by 13.5% at point O compared to point A, while *f* is decreased by 50.6%. *Nu* number is decreased by 27.3% at point B compared to point O, while *f* is decreased by 62.2%, as shown in Table 7. A relatively benefit of heat transfer enhancement is achieved with a relatively small cost of power consumption at point O under the fixed *Re* number. Therefore, point O is applicable in the engineering field. The corresponding optimal parameters of the conical strip at this point are $d_1 = 20.26$ mm, $\alpha = 45.04°$, $\beta = 40.55°$, and $p = 1$.

4.4. Variation of operating conditions

The optimal structural parameters under a fixed *Re* number are determined by the optimized design in the previous subsection, which is based on the optimization principle of improving the actual efficiency. During the practical operation of the PTR, mass flow rates (*M*), inlet temperatures (T_{inlet}), and direct normal irradiances (*DNI*) also have an impact on the system performance. This section focuses on evaluating the comprehensive performance of the system with optimal structural parameters under different operating conditions.

Fig. 17 illustrates the performance differences between enhanced PTR and smooth PTR under different *M* and T_{inlet}, where $DNI = 1000$ W/m^2 and the *Re* number ranges from 5000 to 153000. The heat loss of the PTR increases as T_{inlet} increases. The pump work mainly depends on the magnitude of *M*, while the variation of T_{inlet} has a minor role in power consumption. It is observed from Fig. 17 (a) and (b) that the heat loss of the enhanced PTR is decreased by 6.0%–73.4% and the pump power is decreased by 8.26–13.54 times compared to that of the smooth PTR. In addition, the actual efficiency of the enhanced PTR is increased by 0.2%–3.3% when compared to that of the smooth PTR within the research range, which indicates that the benefit of the heat loss reduction is greater than the cost of the increment in power consumption. The limitation of the wall temperature is one of the core focuses of this study. According to Fig. 17 (d), the maximum wall temperature difference decreases from 46 K-272 K to 27 K–101 K due to the heat transfer enhancement through the conical strip, which can effectively reduce the bending deformation of the absorber tube.

Fig. 18 describes the performance comparisons between the optimal enhanced PTR and the smooth PTR under different *DNI* and *M* when $T_{inlet} = 500$ K and the *Re* number range from 14000 to 136000. The *DNI* determines the volume of heat energy collected by the PTR. The larger *DNI*, the greater the temperature increase of the absorber tube and the

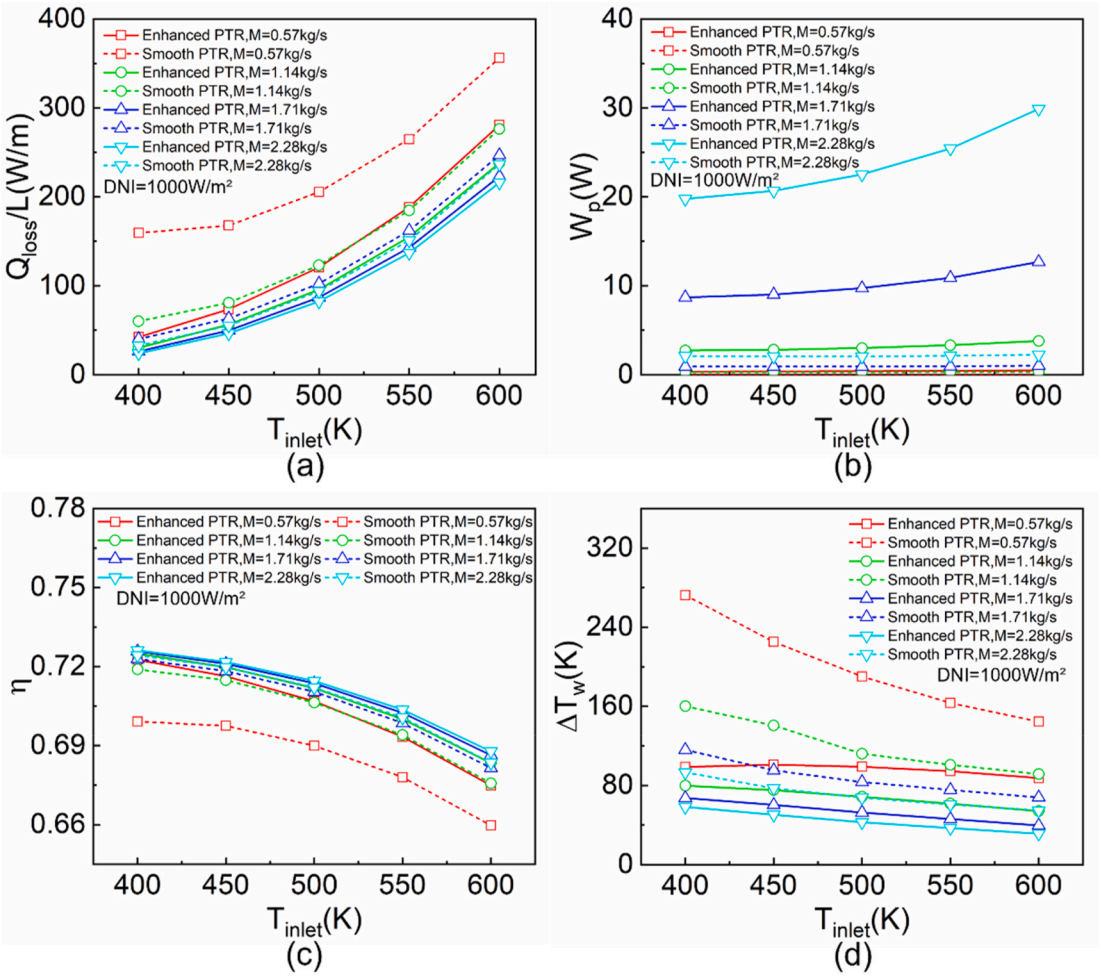

Fig. 17. Performance comparisons of the enhanced PTR and the smooth PTR with inlet temperatures under different mass flow rates: (a) heat loss; (b) pump power; (c) actual efficiency; (d) maximum wall temperature difference.

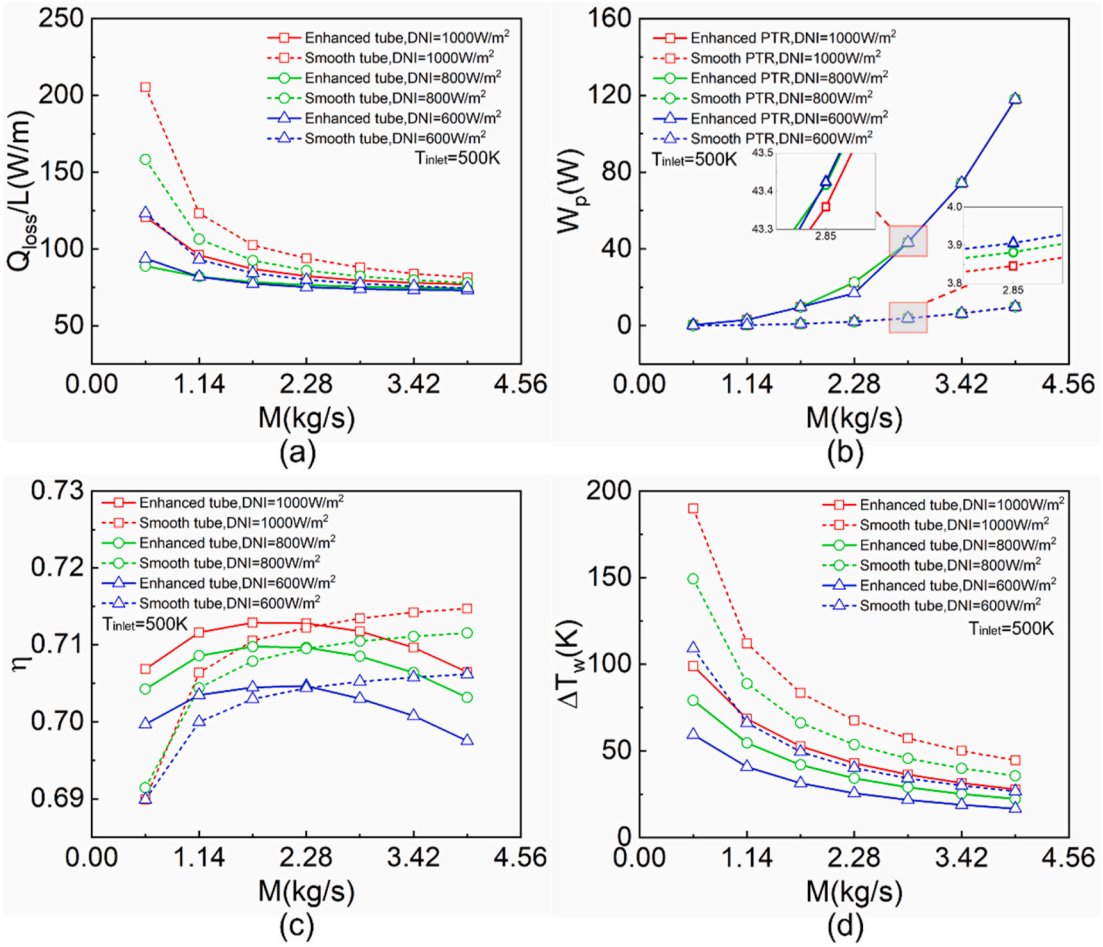

Fig. 18. Performance comparisons of the enhanced PTR and the smooth PTR with mass flow rates under different direct normal irradiances: (a) heat loss; (b) pump power; (c) actual efficiency; (d) maximum wall temperature difference.

poorer the performance of the absorber coating. As shown in Fig. 18 (a), the heat loss increases with the increasing *DNI*. The convective heat transfer performance increases as *M* increases, thus the heat losses of both the enhanced PTR and the smooth PTR are insignificant at high *M*. Besides, the insertion of the conical strip leads to a substantial increase in pump work. The increase in the pump power of the enhanced PTR becomes more pronounced as *M* increases, while the change in *DNI* has almost no effect on the pump power, as seen in Fig. 18 (b). The heat loss of the enhanced PTR is 2.0%–41.2% lower than that of the smooth PTR, and the pump power is increased by 8.97–12.15 times. It is evident from Fig. 18 (c) that the actual efficiency of the enhanced PTR is lower than that of the smooth PTR under high *Re* numbers, which indicates that the enhancement effect of the heat collection by the conical strip is suppressed by the high cost of power consumption. The conical strip inserts are not suitable for moderate- and high-temperature applications in PTRs at high Reynolds numbers due to their lower actual efficiency. Considering the practical application background, i.e., the conditions where the mass flow rate is not too high, the enhanced tube proposed in this study has potential for practical applications. Moreover, the enhanced PTR provides favorable performance in reducing temperature differences, and the maximum wall temperature difference decreases with increasing *M* and decreasing DNI, as observed in Fig. 18 (d).

Based on the second law of thermodynamics, the irreversible loss of the enhanced PTR and the smooth PTR is investigated in this study by using entropy generation and exergy destruction analyses. Fig. 19 gives comparisons of irreversible performance between the optimal enhanced PTR and the smooth PTR under different operating conditions. It can be seen from Fig. 19 (a) and (c) that the entropy generation decreases as T_{inlet} and *M* increase. Furthermore, the smaller *DNI*, the smaller the entropy generation. The trend of the exergy destruction in Fig. 19 (b) and (d) is consistent with the entropy generation, which to some extent confirms the unity of the entropy generation and exergy destruction in describing the irreversible process. Within the study range, the entropy generation of the optimal enhanced PTR is reduced by 22.2%–49.3%, and the exergy destruction is reduced by 30.6%–45.9% when compared to the smooth PTR. The result shows that the conical strip can effectively improve the thermal performance of the PTR and diminish irreversible losses in the heat collecting process.

4.5. Comparison with other studies

To comparatively analyze the performance of the conical strip in this paper, comparisons with previous studies such as wave-tape [11], wall-detached twisted tape [13], perforated plate [15], wire coil [18], perforated ring [21], and conical strips [26–28,31] are carried out and the results are presented in Fig. 20. In consideration of the discrepancies in working fluids, parameter settings, and operating conditions in different papers, the comparison only provides a limited reference. The *Nu* number and the friction factor of the enhanced PTR in this study are moderate among these heat transfer enhancement measures, and the corresponding *PEC* is at the same position. It is demonstrated that the enhanced PTR with a single conical strip inserted has an acceptable overall performance. Besides, the conical strip configuration with a downward impingement in the high heat flux region is more beneficial to the heat collecting process of PTRs compared to other conical inserts. What's more, two or more conical strips are employed to enhance the

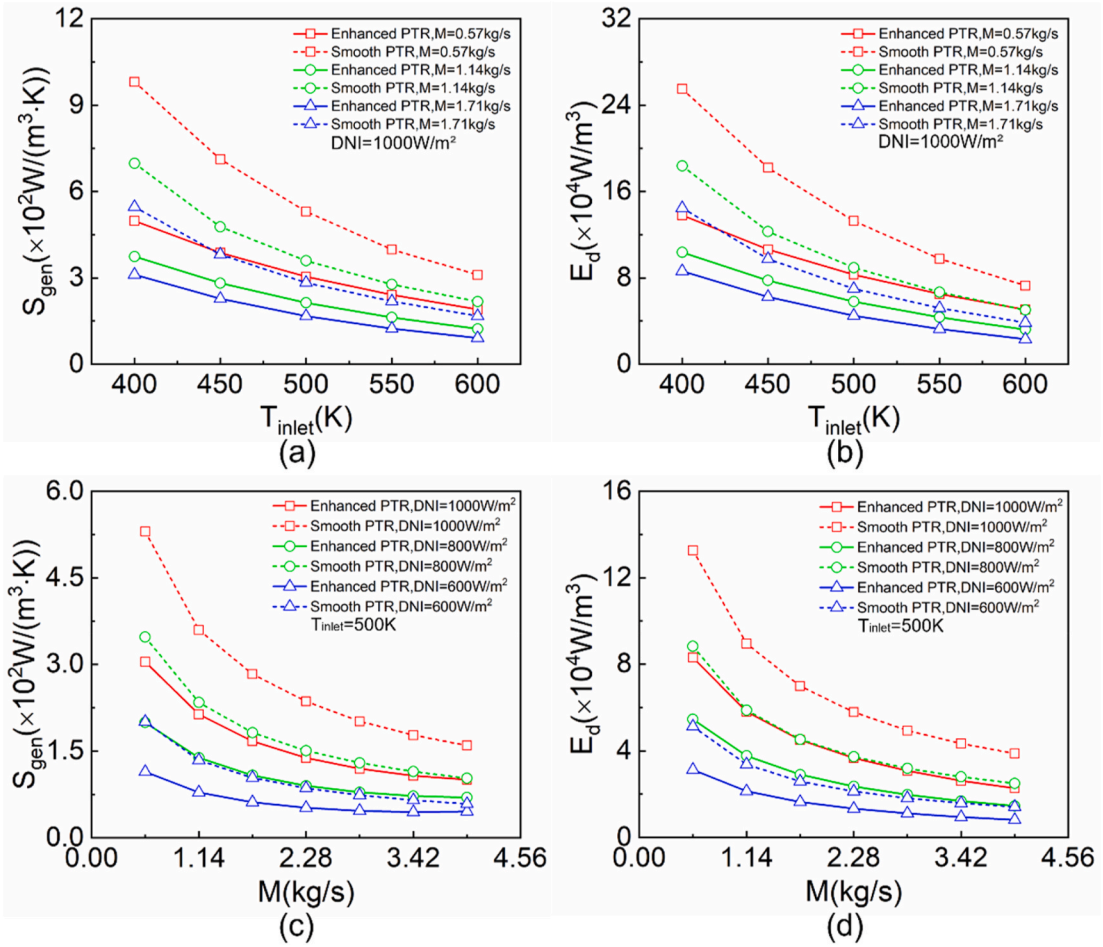

Fig. 19. Irreversible performance comparisons of the enhanced PTR and the smooth PTR under different operating conditions: (a) entropy generation (T_{inlet}); (b) exergy destruction (T_{inlet}); (c) entropy generation (M); (d) exergy destruction (M).

ability of heat transfer in previous works, while the single conical strip has been able to achieve good heat transfer performance while causing a smaller pressure drop loss. It is an advantage to reduce the pump work of PTRs. Therefore, it is promising to use the conical strip configuration proposed in this paper for moderate- and high-temperature applications in PTRs.

5. Conclusion

In this paper, considering the characteristics of highly non-uniform heat flux within the outer surface of the absorber tube, an enhanced PTR with a novel single conical strip is proposed to improve the thermal performance of the solar collector system. The thermal-hydraulic performance and efficiency of the novel PTR are investigated in detail through numerical simulation. Moreover, the optimal combination of parameters of the enhanced PTR is obtained through multi-objective optimization, and its performance is evaluated under different operating conditions. The main conclusions are as follows.

The conical strip can guide the fluid down to the high heat flux region, and two symmetrical longitudinal vortices are formed inside the tube. With this flow field structure, the heat transfer performance of the enhanced PTR is significantly improved, especially in the lower half of the absorber tube. Moreover, the temperature uniformity of the absorber tube for the enhanced PTR is significantly improved compared with that of the smooth PTR, which effectively reduces the thermal strain of the absorber tube and prevents the bending of the absorber tube.

Further, the effects of four structural parameters, namely inner diameter (d_1), central angle (α), inclined angle (β), and pitch ratio(p), on the performance of PTRs are investigated under a fixed Reynolds number. As different parameter combinations bring various effects, multi-objective optimization of the structural parameters is performed by combining ANN and NSGA-II. The optimal structural parameters determined by TOPSIS are $d_1 = 20.26$ mm, $\alpha = 45.04°$, $\beta = 40.55°$, and $p = 1$.

Finally, the performance of the optimal combination of parameters is evaluated under different operating conditions, including mass flow rates (M), inlet temperatures (T_{inlet}), and direct normal irradiances (DNI). Compared to the smooth PTR, the Nu number is increased by 51.7%–131% combined with a 7.75–13.43 times increase in f, and PEC varies from 0.70 to 1.17 for the enhanced PTR within the study range. The tube wall temperature is dropped by up to 168 K, while the heat loss is decreased by 2.0%–73.4%. As M is less than 2.28 kg/s, the actual efficiency of the enhanced PTR is greater than that of the smooth PTR, with a maximum improvement of 3.3%. It is found from the entropy and exergy analysis that the conical strip effectively reduces the irreversibility in the heat collecting process. The entropy generation of the enhanced PTR reduces by 22.2%–49.3%, and the exergy destruction reduces by 30.6%–45.9%.

CRediT authorship contribution statement

Gen Ou: Conceptualization, Methodology, Software, Validation, Formal analysis, Investigation, Data curation, Writing – original draft, Writing – review & editing. **Peng Liu:** Conceptualization, Methodology, Software, Data curation. **Zhichun Liu:** Resources, Supervision, Project administration, Funding acquisition. **Wei Liu:** Resources, Supervision,

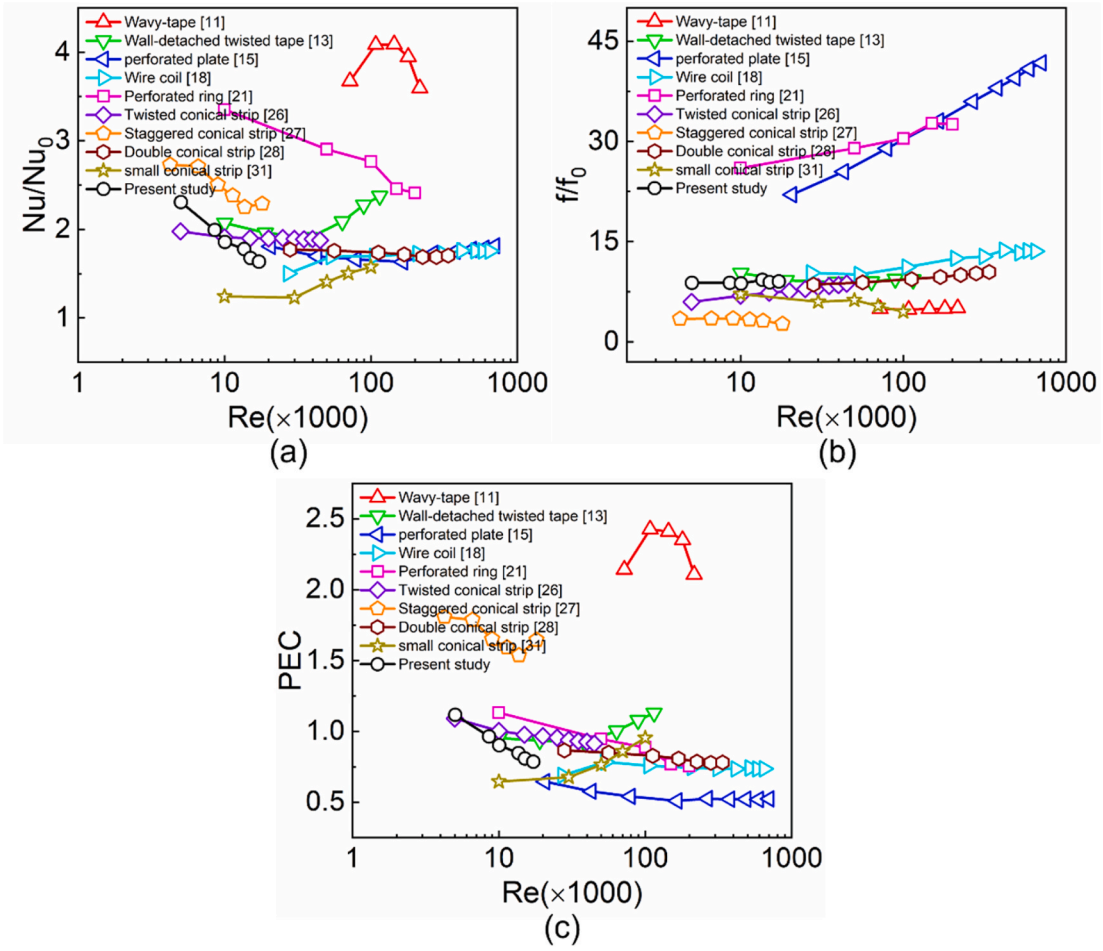

Fig. 20. Comparison with other studies: (a) Nusselt number ratio; (b) friction factor ratio; (c) *PEC*.

Project administration, Funding acquisition.

Declaration of competing interest

The authors declare that they have no known competing financial interests or personal relationships that could have appeared to influence the work reported in this paper.

Acknowledgment

This work was supported by the National Natural Science Foundation of China (Grant No. 51736004).

Nomenclature

a	thermal diffusivity of the fluid, m^2/s
A	area of the parabolic reflector zone, m^2
C_p	specific heat at constant pressure of the fluid, J/(kg·K)
d_1	inner diameter of the conical strip, m
d_2	inner diameter of the conical strip, m
d_{gi}	inner diameter of glass tube, m
d_{go}	outer diameter of glass tube, m
DNI	direct normal irradiance, W/m^2
d_{ri}	inner diameter of absorber tube, m
d_{ro}	outer diameter of absorber tube, m
E_{xd}	total exergy destruction per unit volume of fluid, W/m^3
f	friction factor
h	heat transfer coefficient, $W/(m^2·K)$
h_w	convective heat transfer coefficient of the glass tube to the ambiance, $W/(m^2·K)$
k	kinetic energy, m/s^2
L	overall length of absorber tube, m
M	mass flow rate of the PTR, kg/s
Nu	Nusselt number
Nu_{cir}	circumferential Nusselt number
p	pitch ratio of the conical strip
P	pressure of the fluid, Pa
p^*	pitch of the conical strip, m
PEC	performance evaluation criteria
Pr	Prandtl number of the fluid
Pr_t	turbulent Prandtl number
q_{cir}	circumferential heat flow at the inner wall of the absorber tube, W/m^2
q_{eff}	mean heat flux at the inner wall of the absorber tube, W/m^2
Q_{eff}	heat absorbed by HTF, W
Q_{loss}	system heat loss, W
Q_{solar}	total solar radiation absorbed by the system, W
Re	hydraulic Reynolds number
S_{gen}	total entropy generation per unit volume of fluid, $W/(m^3·K)$
T	temperature of the fluid, K
T_0	ambient temperature, K
T_c	the outer surface temperature of the absorber tube, K
T_{cir}	mean circumferential temperature at the inner wall of the absorber tube, K
T_f	mean temperature of the fluid, K
T_{inlet}	mean temperature of the fluid at the inlet, K
T_w	mean temperature at the inner wall of the absorber tube, K
T_{wmax}	maximum temperature of the absorber tube, K

T_{wmin}	minimum temperature of the absorber tube, K
u	velocity of the fluid, m/s
u_0	ambient wind speed, m/s
u_{in}	mean velocity of the fluid at the inlet, m/s
V	volume of the fluid, m^3
ΔP	pressure drop between the inlet and outlet of the absorber tube, Pa
ΔT_w	maximum wall temperature difference, K
∇T	temperature gradient of the fluid at a certain location, K/m

Greek symbols

α	central angle of the conical strip, °
β	inclined angle of the conical strip, °
Γ	turbulent kinetic energy, m/s^2
ε	turbulent dissipation rate m^2/s^3
ε_c	emissivity of the coating
η_e	power generation efficiency
λ	thermal conductivity of the fluid, W/(m·K)
μ	dynamic viscosity of the fluid, Pa·s
μ_t	turbulent viscosity, Pa·s
ρ	density of the fluid, kg/m^3
σ_k	Prandtl number corresponding to k
σ_ε	Prandtl number corresponding to ε

References

[1] Y.-L. He, Y. Qiu, K. Wang, F. Yuan, W.-Q. Wang, M.-J. Li, J.-Q. Guo, Perspective of concentrating solar power, Energy 198 (2020), 117373.
[2] E. Bellos, C. Tzivanidis, Alternative designs of parabolic trough solar collectors, Prog. Energy Combust. Sci. 71 (2019) 81–117.
[3] M.H. Abedini-Sanigy, F. Ahmadi, E. Goshtasbirad, M. Yaghoubi, Thermal stress analysis of absorber tube for a parabolic collector under quasi-steady state condition, Energy Proc. 69 (2015) 3–13.
[4] N.u. Rehman, M. Uzair, M. Asif, Evaluating the solar flux distribution uniformity factor for parabolic trough collectors, Renew. Energy 157 (2020) 888–896.
[5] E. Bellos, C. Tzivanidis, D. Tsimpoukis, Enhancing the performance of parabolic trough collectors using nanofluids and turbulators, Renew. Sustain. Energy Rev. 91 (2018) 358–375.
[6] N. Basbous, M. Taqi, M.A. Janan, Thermal Performances Analysis of a Parabolic Trough Solar Collector Using Different Nanofluids, International renewable and sustainable energy conference (IRSEC), IEEE, 2016, pp. 322–326.
[7] G. Coccia, G. Di Nicola, L. Colla, L. Fedele, M. Scattolini, Adoption of nanofluids in low-enthalpy parabolic trough solar collectors: numerical simulation of the yearly yield, Energy Convers. Manag. 118 (2016) 306–319.
[8] E.A. Chavez Panduro, F. Finotti, G. Largiller, K.Y. Lervåg, A review of the use of nanofluids as heat-transfer fluids in parabolic-trough collectors, Appl. Therm. Eng. 211 (2022), 118346.
[9] M. Allam, M. Tawfik, M. Bekheit, E. El-Negiry, Heat transfer enhancement in parabolic trough receivers using inserts: a review, Sustain. Energy Technol. Assessments 48 (2021), 101671.
[10] M. Shahzad Nazir, A. Shahsavar, M. Afrand, M. Arıcı, S. Nižetić, Z. Ma, H.F. Öztop, A comprehensive review of parabolic trough solar collectors equipped with turbulators and numerical evaluation of hydrothermal performance of a novel model, Sustain. Energy Technol. Assessments 45 (2021), 101103.
[11] X. Zhu, L. Zhu, J. Zhao, Wavy-tape insert designed for managing highly concentrated solar energy on absorber tube of parabolic trough receiver, Energy 141 (2017) 1146–1155.
[12] X. Song, G. Dong, F. Gao, X. Diao, L. Zheng, F. Zhou, A numerical study of parabolic trough receiver with nonuniform heat flux and helical screw-tape inserts, Energy 77 (2014) 771–782.
[13] A. Mwesigye, T. Bello-Ochende, J.P. Meyer, Heat transfer and entropy generation in a parabolic trough receiver with wall-detached twisted tape inserts, Int. J. Therm. Sci. 99 (2016) 238–257.
[14] S. Ghadirijafarbeigloo, A.H. Zamzamian, M. Yaghoubi, 3-D numerical simulation of heat transfer and turbulent flow in a receiver tube of solar parabolic trough concentrator with louvered twisted-tape inserts, Energy Proc. 49 (2014) 373–380.
[15] A. Mwesigye, T. Bello-Ochende, J.P. Meyer, Heat transfer and thermodynamic performance of a parabolic trough receiver with centrally placed perforated plate inserts, Appl. Energy 136 (2014) 989–1003.
[16] M.T. Jamal-Abad, S. Saedodin, M. Aminy, Experimental investigation on a solar parabolic trough collector for absorber tube filled with porous media, Renew. Energy 107 (2017) 156–163.
[17] K.S. Reddy, K. Ravi Kumar, C.S. Ajay, Experimental investigation of porous disc enhanced receiver for solar parabolic trough collector, Renew. Energy 77 (2015) 308–319.
[18] İ.H. Yılmaz, A. Mwesigye, T.T. Göksu, Enhancing the overall thermal performance of a large aperture parabolic trough solar collector using wire coil inserts, Sustain. Energy Technol. Assessments 39 (2020), 100696.
[19] O. Chakraborty, B. Das, R. Gupta, Impact of helical coil insert in the absorber tube of parabolic trough collector, Springer, Model. Simulat. Optimiz. (2021) 177–187.
[20] K. Arshad Ahmed, E. Natarajan, Thermal performance enhancement in a parabolic trough receiver tube with internal toroidal rings: a numerical investigation, Appl. Therm. Eng. 162 (2019), 114224.
[21] A. Mahmoudi, M. Fazli, M.R. Morad, E. Gholamalizadeh, Thermo-hydraulic performance enhancement of nanofluid-based linear solar receiver tubes with forward perforated ring steps and triangular cross section; a numerical investigation, Appl. Therm. Eng. 169 (2020), 114909.
[22] H.A. Mohammed, H.B. Vuthaluru, S. Liu, Heat transfer augmentation of parabolic trough solar collector receiver's tube using hybrid nanofluids and conical turbulators, J. Taiwan Inst. Chem. Eng. 125 (2021) 215–242.
[23] A. Fan, J. Deng, J. Guo, W. Liu, A numerical study on thermo-hydraulic characteristics of turbulent flow in a circular tube fitted with conical strip inserts, Appl. Therm. Eng. 31 (14–15) (2011) 2819–2828.
[24] P.W. Deshmukh, R.P. Vedula, Heat transfer and friction factor characteristics of turbulent flow through a circular tube fitted with vortex generator inserts, Int. J. Heat Mass Tran. 79 (2014) 551–560.
[25] W. Liu, P. Liu, J.B. Wang, N.B. Zheng, Z.C. Liu, Exergy destruction minimization: a principle to convective heat transfer enhancement, Int. J. Heat Mass Tran. 122 (2018) 11–21.
[26] M. Pourramezan, H. Ajam, Modeling for thermal augmentation of turbulent flow in a circular tube fitted with twisted conical strip inserts, Appl. Therm. Eng. 105 (2016) 509–518.
[27] S. Jafar Kutbudeen, M. Arulprakasajothi, B. N, K. Elangovan, Effect of conical strip inserts in a parabolic trough solar collector under turbulent flow, Energy Sources, Part A Recovery, Util. Environ. Eff. 44 (1) (2019) 2556–2568.
[28] P. Liu, N. Zheng, Z. Liu, W. Liu, Thermal-hydraulic performance and entropy generation analysis of a parabolic trough receiver with conical strip inserts, Energy Convers. Manag. 179 (2019) 30–45.
[29] M. Bahiraei, K. Gharagozloo, H. Moayedi, Experimental study on effect of employing twisted conical strip inserts on thermohydraulic performance considering geometrical parameters, Int. J. Therm. Sci. 149 (2020), 106178.
[30] M. Bahiraei, Z. Rahimi, F. Nazari, A combined multi-criterion optimization to determine optimum geometrical parameters for flow of an ecofriendly graphene-based nanofluid inside tube enhanced with twisted conical strip inserts, Powder Technol. 377 (2021) 336–349.
[31] N. Abed, I. Afgan, A. Cioncolini, H. Iacovides, A. Nasser, Effect of various multiple strip inserts and nanofluids on the thermal–hydraulic performances of parabolic trough collectors, Appl. Therm. Eng. 201 (2022), 117798.
[32] H.-Z. Han, B.-X. Li, H. Wu, W. Shao, Multi-objective shape optimization of double pipe heat exchanger with inner corrugated tube using RSM method, Int. J. Therm. Sci. 90 (2015) 173–186.
[33] S. Khanmohammadi, N. Mazaheri, Second law analysis and multi-criteria optimization of turbulent heat transfer in a tube with inserted single and double twisted tape, Int. J. Therm. Sci. 145 (2019), 105998.
[34] M. Yang, B.-Y. Cao, Multi-objective optimization of a hybrid microchannel heat sink combining manifold concept with secondary channels, Appl. Therm. Eng. 181 (2020), 115592.
[35] Z. He, Y. Yan, T. Zhao, L. Zhang, Z. Zhang, Multi-objective optimization and multi-factors analysis of the thermal/hydraulic performance of the bionic Y-shaped fractal heat sink, Appl. Therm. Eng. 195 (2021), 117157.
[36] V.E. Dudley, G.J. Kolb, A.R. Mahoney, T.R. Mancini, C.W. Matthews, M. Sloan, D. Kearney, Test Results: SEGS LS-2 Solar Collector, Sandia National Lab.(SNL-NM), Albuquerque, NM (United States), 1994.
[37] T.-H. Shih, W.W. Liou, A. Shabbir, Z. Yang, J. Zhu, A new k-ε eddy viscosity model for high Reynolds number turbulent flows, Comput. Fluid 24 (3) (1995) 227–238.
[38] P. Liu, Z. Dong, H. Xiao, Z. Liu, W. Liu, Thermal-hydraulic performance analysis of a novel parabolic trough receiver with double tube for solar cascade heat collection, Energy 219 (2021), 119566.
[39] Y.-L. He, J. Xiao, Z.-D. Cheng, Y.-B. Tao, A MCRT and FVM coupled simulation method for energy conversion process in parabolic trough solar collector, Renew. Energy 36 (3) (2011) 976–985.
[40] A.M. Delgado-Torres, L. García-Rodríguez, Comparison of solar technologies for driving a desalination system by means of an organic Rankine cycle, Desalination 216 (1–3) (2007) 276–291.
[41] R. Forristall, Heat Transfer Analysis and Modeling of a Parabolic Trough Solar Receiver Implemented in Engineering Equation Solver, National Renewable Energy Lab., Golden, CO.(US), 2003.
[42] S. Mullick, S. Nanda, An improved technique for computing the heat loss factor of a tubular absorber, Sol. Energy 42 (1) (1989) 1–7.
[43] H. Xiao, P. Liu, Z. Liu, W. Liu, Performance analyses in parabolic trough collectors by inserting novel inclined curved-twisted baffles, Renew. Energy 165 (2021) 14–27.
[44] V. Gnielinski, New equations for heat and mass transfer in turbulent pipe and channel flow, Int. Chem. Eng. 16 (2) (1976) 359–368.
[45] B. Petukhov, Heat transfer and friction in turbulent pipe flow with variable physical properties, Elsevier, Adv. Heat Tran. (1970) 503–564.
[46] S. Kandlikar, S. Garimella, D. Li, S. Colin, M.R. King, Heat Transfer and Fluid Flow in Minichannels and Microchannels, elsevier, 2005.

[47] A. Zendehboudi, X. Li, Desiccant-wheel optimization via response surface methodology and multi-objective genetic algorithm, Energy Convers. Manag. 174 (2018) 649–660.
[48] K. Deb, A. Pratap, S. Agarwal, T. Meyarivan, A fast and elitist multiobjective genetic algorithm: NSGA-II, IEEE Trans. Evol. Comput. 6 (2) (2002) 182–197.
[49] H. Allouhi, A. Allouhi, A. Jamil, Multi-objective optimization of a CSP-based dish Stirling field layout using Genetic Algorithm and TOPSIS method: case studies in Ouarzazate and Madrid, Energy Convers. Manag. 254 (2022), 115220.